Acoustic fields and microfluidic patterning around embedded micro-structures subject to surface acoustic waves

Acoustic fields and microfluidic patterning around embedded micro-structures subject to surface acoustic waves

David J. Collins[*†], Richard O'Rorke[2†], Adrian Neild[3], Jongyoon Han[4,5], Ye Ai[2*]

[1]Department of Biomedical Engineering, The University of Melbourne, Melbourne, Victoria 3010, Australia

[2]Pillar of Engineering Product Development, Singapore University of Technology and Design, Singapore 487372, Singapore

[3]Department of Mechanical and Aerospace Engineering, Monash University, Melbourne, VIC 3800, Australia

[4]Department of Biological Engineering, Massachusetts Institute of Technology, Cambridge, MA 02139, USA

[5]Department of Electrical Engineering and Computer Science, Massachusetts Institute of Technology, Cambridge, MA 02139, USA

† These authors contributed equally to this work.

* Corresponding authors. Email: aiye@sutd.edu.sg; Tel: (+65) 6499 4553, Email: david.collins@unimelb.edu.au; Tel: (+61) 3 8344 0867

Abstract

Recent research has shown that interactions between acoustic waves and microfluidic channels can generate microscale interference patterns with the application of a traveling surface acoustic wave (SAW), effectively creating standing wave patterns with a traveling wave. Forces arising from this interference can be utilized for precise manipulation of micron-sized particles and biological cells. The patterns that have been produced with this method, however, have been limited to straight lines and grids from flat channel walls, and where the spacing resulting from this interference has not previously been comprehensively explored. In this work we examine the interaction between both straight and curved channel interfaces with a SAW to derive geometrically deduced analytical models. These models predict the acoustic force-field periodicity near a channel interface as a function of its orientation to an underlying SAW, and are validated with experimental and simulation results. Notably, the spacing is larger for flat walls than for curved ones and is dependent on the ratio of sound speeds in the substrate and fluid. Generating these force-field gradients with only travelling waves has wide applications in acoustofluidic systems, where channel interfaces can potentially support a range of patterning, concentration, focusing and separation activities by creating locally defined acoustic forces.

1. Introduction

Microscale acoustics have a wide range of biomedical applications where cell manipulation is required. Cells, spheroids, droplets and particles can be patterned[1–3], sorted[4–7], separated[8–10], concentrated[11–13], focused[14,15] and otherwise manipulated[16,17] with application of biocompatible[18–20] acoustic forces. The acoustic radiation force is a phenomenon of nonlinear acoustics that can be used to translate objects at the microscale. Surface acoustic waves (SAW) are a particularly useful set of actuation wave modes as they can readily define the locations where acoustic forces are realized with potential for multiple addressable transducers[21,22], create fields that evolve spatially with different transducer designs[23–25] and contain nodal positions that can be defined by the applied phase[26–29] or in select sub-regions along the propagation direction[30]. Moreover, SAW transducers can readily be bonded to conventional 2D microfluidic devices and can efficiently couple acoustic energy into an overlaying fluid domain.

The physics of these systems have been extensively explored, where the effects of acoustic streaming[31–35] and acoustic radiation forces arising from standing waves[36–39] and travelling waves[40–42] have been well accounted for. These models, however, are largely predicated on the existence of spatially periodic acoustic fields along the propagation direction without accounting for the effect of channel elements in the SAW path. With the exception of the so-called anechoic corner, where total internal reflection (TIR) at the channel-fluid interface results in an acoustic void near the channel interface[43,44], the effects of channel interfaces on the acoustic field remain largely unexplored. Only recently has it been shown that TIR at the channel edge has an effect across the entire fluid domain, where diffractive interference patterns arise from the imposition of a channel-bounded travelling SAW[45]. TIR occurs when a wavefront propagates between domains with different sound speeds. In the case of a

combination of materials such as polydimethylsiloxane (PDMS) and water, where the PDMS sound speed (c_{PDMS} = 1030 m/s) is lower than that of water ($c_l \approx$ 1500 m/s), wavefronts intersecting this boundary from any point above a critical angle $\theta_c = \sin^{-1}\frac{c_{\mathrm{PDMS}}}{c_l} \approx 43°$ (measured from the transducer plane) are entirely reflected and do not contribute to the acoustic field in the fluid. Since the acoustic wavefronts typically propagate from the substrate into PDMS at a Rayleigh angle (θ_R) less than θ_c, approximately 22° for water on lithium niobate, it has been shown that a PDMS channel wall acts as an effective boundary that limits the extent of the SAW transducer domain in a microchannel[43,46]. Recently work noted the existence of an interference-based fringe pattern near channel walls that were orthogonal[45] and parallel[47] to the propagation direction, respectively. O'Rorke *et al.* also demonstrated a meshless quasi-analytical model based on the assumption that the pressure magnitude at a given point in the fluid is equal to the sum contribution from spherically expanding wavelets emanating from a finite transducer area[48]. Interestingly, this work shows that particle patterns can be generated without the imposition of a standing SAW, where time-averaged acoustic periodic fringe spacing arises from diffractive effects associated with a spatially limited transducer domain. This contrasts somewhat with work from Leibacher *et al.* that demonstrated PDMS walls had negligible acoustic effects[49], permitting particle patterning in fluid domains that are a subset of the resonant wall dimensions. This particular case differs from the aforementioned demonstration of channel-induced patterning in SAW devices, however, since in standing-wave resonant acoustic fields the intersecting wavefronts travel perpendicular to the water/PDMS interface, at an angle greater than θ_c, and are thus not subject to TIR. It is possible to generate strong fringe patterns with traveling SAW, however, because the wave propagation direction through the fluid is less than the critical angle ($\theta_R < \theta_c$), causing TIR. For other common potential polymer channel materials including polymethyl methacrylate (PMMA), polycarbonate and polystyrene, all with sound speeds greater than water, the condition $\theta_R <$

θ_c is not met, and acoustic energy can couple into the fluid at all points along the channel height. While fringe patterns would still result (since a portion of the acoustic energy traveling toward the polymer/fluid interface is still be reflected back into the polymer), the transducer extent would not be as effectively limited as would be the case where all the acoustic energy is reflected ($\theta_R < \theta_c$).

Micropillar waveguides can also be used to effectively constrain the transducer domain for localized acoustic effects with SAW as the actuation source, where a pillar/post is used to couple acoustic energy to selected microchannel regions[48,50–52]. Rambach et al. demonstrated the use of this approach to create particle patterning on top of a waveguide with just a travelling wave[51], though predictive analytical equations that describe pattern spacings have yet to be developed. Directly using channel wall TIR effects instead, however, presents a ready avenue for creating particle patterns that are inherently aligned with channel features while avoiding the additional alignment and bonding steps that using a waveguide layer entails. Since channel walls are essentially ubiquitous in microfluidic SAW, it is in any case important to account for the effects that their presence will have on the acoustic field and resultant particle patterning. Using only travelling waves to generate periodic spacings not only simplifies device setup and design compared to waveguide and standing SAW devices, but also couples particle actuation to the channel geometry rather than just the underlying SAW, allowing for highly localized patterning and focusing activities that can be incorporated by shaping the channel features. The analytical models that have thus far been developed to predict the interference patterns, however, are limited to specific channel interface angles (parallel and orthogonal, $\theta = 0°$ and $\theta = 90°$, with respect to the SAW propagation direction). To build a more complete understanding of channel interface effects on the surrounding acoustic field, in this work we develop generalized acoustic interaction models for channel interfaces subject to a travelling

substrate wave to predict acoustic field periodic fringe spacing.

A conceptual image showing interference patterns is presented in Figure 1a, where the interaction of SAW wavefronts from a substrate-bound wave and fluid wavefronts from a channel interface in its path results in force potential minima locations in the fluid. Figure 1b shows the effect of channel walls in representative experimental cases, including curved (i and ii) and straight channel interfaces (iii). Though the air gaps shown here are useful in limiting SAW attenuation, where the substrate-air interface is much less attenuating than the substrate-PDMS one, this is not necessary to produce patterning effects around channel interfaces due to TIR at the PDMS/water interface. In this work we show that channel walls can be used to generate locally defined acoustic fields from travelling SAW with arbitrary wall orientations, useful for flexible acoustic micropatterning, and develop analytical models that predict the acoustic field periodicity used to drive micromanipulation in these systems. In doing so we explicitly demonstrate for the first time that channel curvature can impact periodicity and accordingly derive and test analytical models that can predict diffractive periodicity in SAW-based microfluidic devices.

2. Principles

In this work we apply the well-understood physical concepts of the Huygens-Fresnel principle and the linear superposition of wavefronts in order to develop novel predictive models that describe particle patterning in microfluidic devices actuated by SAW. A consequence of the Huygens-Fresnel principle, which states that a wavefront is the sum of all wavelet contributions from the extent of a wave source, is that a finite transducer area appears to generate spherical wavelets that emanate from the transducer edges. These wavelets have been visualized experimentally as edge waves with short-duration pulses[53,54]. In the case of oscillatory acoustic

waves, these wavelets are more appropriately thought of as a 'virtual field' that represents negative wavefront contributions from all regions outside of the transducer domain that then interfere with the planar wavefronts from the transducer. This principle is briefly illustrated in Supplementary Figures S1 and S2, where the field emitted from a finite transducer width is equivalent to the sum of planar wavefronts with the 180° out-of-phase wavelets emanating from everywhere outside of transducer region. In the case of a SAW coupling into an overlaying fluid, the transducer boundaries are defined by the channel walls, resulting in 180° out-of-phase wavelets from the edges that coalesce into fluid wavefronts. These interfere with the classical planar wavefronts emanating from the substrate. These latter wavefronts we term "SAW wavefronts" to highlight that their wavelength and sound speed (as measured in the *x*-*y* plane) is equivalent to that of the underlying substrate wave. Devendran *et al.* examined the case where the channel wall was parallel to the advancing SAW wavefronts, finding that the spacing between subsequent force potential minima is a straightforward function of the acoustic wavelength and the sound speeds in the substrate and fluid[45]. Collins *et al.* studied the case where channel walls were instead parallel to the SAW propagation direction, where limiting the transducer area with channel walls resulted in a two-dimensional particle grid with the imposition of only a one-dimensional standing SAW[46]. Whereas these publications explored the mechanism that gives rise to fringe patterns and used this for particle manipulation at select channel orientations, this present work seeks to establish a comprehensive theory of channel wall interactions and to examine the full range of channel wall orientations (θ). In doing so, we develop models to predict the fringe spacing, λ_θ, as a function of θ with respect to the SAW propagation direction (along the $+x$ direction) and the interface curvature. These 2D models are formulated in the transducer plane (the x-y plane), appropriate given the high aspect ratio of the channels used in this work (which are wide and relatively shallow) to observe these fringes and this being the plane on which microfluidic devices are usually observed,

namely in a top-down or inverted microscope. While these models are appropriate for the cases we consider, with channel heights on the order of the acoustic wavelength or smaller, the acoustic field also evolves in the z-direction with minor changes in the fringe spacing for increasing z and close to a channel boundary; we discuss this in the interpretation of our results in our Results section.

In the case of a channel wall with curvature radii much smaller than the SAW wavelength (with $R \to 0$, where R is the radius of curvature), the value of $\lambda_{\theta}^{(R\to 0)}$ can be predicted by determining the distance from the channel interface that an incoming SAW wavefront (travelling at c_s) will interfere with a fluid wavefront (travelling at c_l). It is intuitive that λ_θ will vary for different θ, with smaller values when the waves are travelling in opposite directions than when they are co-travelling. This concept is illustrated in Figure 2a, which shows how the intersection between a SAW wavefront and a fluid wavefront results in an ellipsoidal interference pattern. This is further illustrated in Supplementary Video 1, which plots the modelled intersection of an expanding fluid wavefront and a series of SAW wavefronts for circular channel features, with R = $0.1\lambda_{\mathrm{SAW}}$, $0.5\lambda_{\mathrm{SAW}}$, $1\lambda_{\mathrm{SAW}}$ and $2\lambda_{\mathrm{SAW}}$. The value of $\lambda_{\theta}^{(R\to 0)}$ for a given θ value can be found by calculating the time taken for these two waves to intersect, which is longer when these wavefronts are traveling in the same direction (θ = 0), and shorter when they are travelling in opposite directions (θ = 180°). At their intersection these wavefronts will destructively interfere, since the fluid wavelets are 180° out of phase with the SAW. Because a travelling SAW is periodic, these intersections will occur at consistent locations, resulting in a periodic series of nodal and antinodal positions radiating outward from the channel feature. The periodicity of this interference pattern can be defined in terms of the acoustic wavelength in the liquid, $\lambda_l = \frac{c_l}{c_s}\lambda_{\mathrm{SAW}}$, and the liquid and substrate sound speeds, with

$$\lambda_\theta^{(R\to 0)} = \frac{\lambda_l}{\left(1 - \frac{c_l}{c_s}\cos\theta\right)}. \qquad \text{Eqn. 1}$$

The derivation for Equation 1 is given in Supplementary Note 1. For simplicity, only one SAW wavefront-channel interaction is shown in Figure 2a. This spacing is conserved for subsequent interactions between any given fluid wavelets and further SAW wavefronts. It is relatively simple to calculate this spacing because the wavelet source is co-located with the object centre regardless of θ (when $R \to 0$). While this condition (in the Rayleigh scattering regime) is an interesting case, channel walls and interfaces are, however, most often either flat or have a finite and observable shape. This simultaneous co-location of wavelet source and SAW wavefront cannot be assumed for flat walls, as the origin of the expanding wavelet that coheres at the intersection point differs from the point where the wavefront and the interface intersect. This is shown conceptually in Figure 2b for the case where $R \to \infty$ (a flat interface). The periodicity of an interference pattern in the vicinity of a channel interface can be solved through straightforward trigonometry, with

$$\lambda_\theta^{(R\to\infty)} = \lambda_l \sin(\theta)\csc(\theta - \theta_I(\theta)), \qquad \text{Eqn. 2}$$

where $csc(\theta)$ is the cosecant of θ and $\theta_I(\theta)$ is the intersection angle, given by

$$\theta_I(\theta) = \sin^{-1}\left(\frac{c_l}{c_s^*(\theta)}\right), \qquad \text{Eqn. 3}$$

which describes the angle at which a coherent fluid wavefront projects from the channel wall (Figure 2b). This is analogous to the definition of the Rayleigh angle, $\theta_R(\theta) = \sin^{-1}(c_l/c_s)$, which describes the angle at which fluid wavefronts project from travelling substrate waves into an adjoining fluid domain; when the sound speed in the fluid domain is less than that of the SAW phase velocity, the wavefronts propagate at an angle from the substrate into the fluid. The key difference here is that the substrate wave velocity $c_s^*(\theta)$ is instead the speed of a

travelling substrate wave intersecting with a channel wall angled at θ. Importantly, this value will change with θ, and is expressed as

$$c_s^*(\theta) = \frac{c_s}{\sin(\theta)}. \qquad \text{Eqn. 4}$$

This means that while $c_s^*(\theta)$ is equal to the sound speed in the substrate at $\theta = 90°$, as θ approaches 0° or 180° $c_s^*(\theta)$ approaches infinity in an analogous manner to the "lighthouse" or "scissors" paradox. In the scissors paradox, for example, from the perspective of the person holding the scissors the contact point between the sufficiently long scissor halves can achieve superluminal velocities as the angle between them approaches zero; the intersection point between the SAW wavefront and the channel wall can similarly achieve arbitrarily high velocities for small angles between the two. For reference, the scissors paradox is resolved since special relativity is not actually violated, as information still cannot travel faster than the speed of light.

Substituting these expressions into Equation 2 we arrive at the expression that predicts the fringe spacing as $R \to \infty$, with

$$\lambda_\theta^{(R\to\infty)} = \lambda_l \sin(\theta) \csc\left(\theta - \sin^{-1}\left(\frac{c_l}{c_s} sin\,\theta\right)\right). \qquad \text{Eqn. 5}$$

The full derivation for Equation 5 is given in Supplementary Note 2. These expressions (Equation 1 and 2) describe models at either extreme (with $R \to 0$ and $R \to \infty$) and demonstrate that the interface curvature influences the fringe spacing. Both expressions for λ_θ described here denote the distance between subsequent SAW wavefront and wavelet intersections, where this spacing is equivalent to the distance between acoustic force potential minima; this is discussed in detail in the next section. Figure 3 examines the behaviour of these models for different sound speed ratios, $\tilde{c} = c_l c_s^{-1}$. While the models in Equation 1 and 2 are equivalent for the separate cases of θ = 0° and θ = 180° $\left(\lambda_{0°}^{(R\to0)} = \lambda_{0°}^{(R\to\infty)}\right.$ and $\lambda_{180°}^{(R\to0)} =$

$\lambda_{180°}^{(R\to\infty)}\Big)$, discrepancies occur at intermediate values of θ and increase for higher values of $\tilde{c}$. For a value of $\tilde{c} = 0.39$, representative of a $LiNbO_3$ substrate and a particle-laden H_2O liquid (with $c_l = 1540$ m/s and $c_s = 3931$ m/s), the maximum difference between these models is equivalent to approximately $0.08\lambda_{\theta}^{(R\to\infty)}$ at $\theta = \pm 78°$. While the difference between these models is small for most intermediate angles, this discrepancy is nevertheless manifested and measurable.

The expressions in Equations 1-5 are predicated on the intersection of linear (first order) pressure fields in the fluid. Because these pressure fields are oscillatory in nature, the time average of these first order fields is necessarily zero. As we will see in the next section, however, these linear pressures give rise to a (time-averaged) nonlinear acoustic force field that can be used to pattern microparticles, where the spacings between individual acoustic force potential minima along which particles aggregate are equal to λ_θ. In the following theory, experiments and simulations, we show how a spatially limited transducer gives rise to a nonuniform acoustic radiation force distribution and demonstrate the power of these models for predicting interference patterns near channel features subject to a travelling SAW.

3. Acoustic Model

To map the acoustic forces in the fluid we must consider the distribution of the oscillatory velocities in the fluid domain. In the case of a spatially limited transducer domain, we can find the value of the fluid oscillation velocities through the sum of contributions from the substrate and the wavelets from the channel wall. The first of these, the wavefronts propagating from the substrate surface into the fluid domain (the SAW wavefronts), are well characterised and have (first order) fluid particle velocities of v_s propagating in the fluid at an angle $\theta_R =$

$\sin^{-1}(c_l/c_s)$, with θ_R measured with respect to the vertical axis. The first order fluid velocities are given by[55,56]

$$v_s = A(x,z)\omega\xi_0 e^{i\omega t} e^{-i(k_s x_\theta \cos\theta)} e^{-k_l z}, \quad \text{Eqn. 6a}$$

$$A = e^{(-\alpha(x_\theta - z\tan\theta_R) - \beta z \sec\theta_R)\cos\theta}, \quad \text{Eqn. 6b}$$

where k_s, k_l are the wavenumbers in the substrate and liquid, θ is the angle of the channel wall, ω is the angular frequency, ξ_0 is the displacement magnitude, x_θ is the direction perpendicular to the channel wall, and the $\cos\theta$ term above accounts for the different SAW propagation directions along x_θ. In the case of $\theta = 0°$, for example, x_θ (and the SAW propagation direction) is in the +x direction, whereas it is the -x direction when $\theta = \pi$. The parameter A can take on values between 0 and 1 and accounts for attenuation at the substrate/fluid interface and in the fluid itself via the terms α and β, respectively[56]. Equation 7b has been modified from this reference to account for different values of θ. These attenuation parameter values are given by

$$\alpha = \frac{\rho_l c_l}{\rho_s c_s \lambda_{SAW}} \quad \text{Eqn. 7a}$$

$$\beta = \frac{b\omega^2}{\rho_l c_l^3}, \quad \text{Eqn. 7b}$$

where $b = \frac{4}{3}\mu + \mu'$, with μ and μ' being the fluid viscosity and bulk viscosity, respectively. These are temperature-dependent values[57], with $\mu = 8.9\times10^{-4}$ Pa·s and $\mu' = 2.5\times10^{-3}$ Pa·s at 25 C° and $\mu = 6.5\times10^{-4}$ Pa·s and $\mu' = 1.8\times10^{-3}$ Pa·s at 40 C°. Regardless, for the devices used here the attenuation along the substrate has a greater effect than that in the fluid; whereas the attenuation length $\alpha^{-1} \approx 12\lambda_{SAW}$ for water on lithium niobate[58], the value of β^{-1} (the attenuation length in the fluid) is at least an order of magnitude larger for frequencies less than 100 MHz[59]. This is seen in Figure 4a, where the attenuation in the z-direction is almost

unnoticeable whereas the wavefront magnitude is appreciably smaller at the right edge of the domain.

The second contribution arises from channel features which limit the spatial extent of the transducer, and act as a virtual source of wavelets. These wavelets represent the wave components that would otherwise have propagated from regions outside of the transducer but are instead blocked by TIR at the channel features, hence they are assigned an opposite phase to the planar wavefronts in Equation 6, noting again that the final acoustic field magnitude can be computed from the sum of planar wavefronts with phase 0° and the 180° out-of-phase fluid wavelets (Supplementary Figure S1). These wavelets combine to form an acoustic beam projecting from the substrate at θ_R representing contributions from outside the channel domain. A complete solution for this acoustic field would require a numerical simulation to determine the specific beam profile. For high aspect ratio channels (width>height) and/or small θ_R, however, it is only the expanding wavelet components travelling mostly parallel to the substrate that gives rise to the interference fringes in the channel domain. This permits the development of a straightforward 2D analytical solution in the x-z plane by approximating the sum of these virtual wavelets as spherically propagating wavefronts emanating from the channel edge adjoining the transducer. We examine here the case of a flat channel wall, in which the spherically propagating wavelets combine into cylindrical wavefronts that have equal magnitude along the length of the channel wall. These first order cylindrical wavefront velocities are given by

$$v_c = D(\theta_h, r)\omega\xi_0 e^{i\omega t} e^{-i(k_l^* r - \pi)} e^{-\beta r}, \qquad \text{Eqn. 8}$$

where θ_h and r define a position in polar coordinates, whose coordinate transformation into the coordinate system of Equation 6 (the x-y plane) is calculated using $\theta_h = \tan^{-1} z/x_\theta$ and $r = \sqrt{{x_\theta}^2 + z^2}$, where x_θ is the axis perpendicular to the channel wall in the plane of the

transducer. The pressure arising from these velocities are plotted in Figure 4b. The value of the fluid wavenumber, $k_l^* = 2\pi/\lambda_l^*$, accounts for the marginally longer path length between the source of the wavelets on a flat wall and the intersection point with a SAW wavefront, where λ_l^* can be found geometrically (see Figure 2b), with $\lambda_l^* = \lambda_l/\cos(\theta_I(\theta)) = \lambda_l[\cos(\sin^{-1}(c_l/c_s \sin(\theta)))]^{-1}$.

The diffraction coefficient $D(\theta_h, r)$ describes the amplitude variation of the contributions from outside the channel; setting the edge of the channel feature at $x_\theta = 0$, these will have a finite amplitude distribution across the channel domain between 0 and 1. While the amplitude of $D(\theta_h, r)$ can be determined through numerical simulation, the Lee coefficients in Equation 9a provide a good approximation, with[60,61]

$$D(\theta_h, r) = \begin{cases} 1, & \upsilon < -1 \\ 0.5 - 0.62\upsilon, & -1 \geq \upsilon \geq 0 \\ 0.5e^{-0.95\upsilon}, & 0 \geq \upsilon > 1 \\ 0.4 - \sqrt{0.1184 - (0.38 - 0.1\upsilon)^2}, & 1 \geq \upsilon > 2.4 \\ \dfrac{0.225}{\upsilon}, & \upsilon > 2.4 \end{cases}, \quad \text{Eqn. 9a}$$

$$\upsilon = r\cos(\theta_h + \theta_R \cos\theta)\sqrt{\frac{2}{r\lambda_l}}, \quad \text{Eqn. 9b}$$

where υ (upsilon) is the Fresnel-Kirchoff parameter, which is a measure of the distance from the channel boundary. This factor υ and the value of $D(\theta_h, r)$ are mapped in Figure S3. The factor $\cos\theta$ accounts for the orientation of the acoustic beam emanating from outside the channel region; these wavefront contributions from outside the channel represented by Equation 8 are subtracted from the wavefronts in Equation 6. For θ = 0°, the acoustic beam is oriented along θ_R (into the channel), whereas for θ = 180° the acoustic beam contribution is pointed away from the channel ($-\theta_R$ along the axis x_θ). While this factor is included for completeness, the contribution from the $[\theta_R \cos\theta]$ term is negligible for distances far from the channel wall and close to the substrate.

The first order pressure components for the SAW wavefronts and cylindrical fluid wavefronts are found with $p_\mathrm{s} = \rho_0 c_l v_\mathrm{s}$ and $p_\mathrm{c} = \rho_0 c_l v_\mathrm{c}$, respectively. Adding these yields the total first order pressure, with $p_1 = p_\mathrm{s} + p_\mathrm{c}$, as shown in Figure 4c. While the scalar pressure fields can be directly summed, doing so for the velocity field must consider the orientation of the vector fields, summing the contributions in the x and z directions independently. The interference velocity magnitude is given by $|\boldsymbol{v}_1| = \sqrt{\left(v_{\mathrm{s}(x)} + v_{\mathrm{c}(x)}\right)^2 + \left(v_{\mathrm{s}(z)} + v_{\mathrm{c}(z)}\right)^2}$, where $v_{\mathrm{s}(x)} = v_\mathrm{s}\sin(\theta_\mathrm{R})$, $v_{\mathrm{s}(z)} = v_\mathrm{s}\cos(\theta_\mathrm{R})$, $v_{\mathrm{c}(x)} = v_\mathrm{c}\cos(\theta_\mathrm{h})$ and $v_{\mathrm{c}(x)} = v_\mathrm{c}\sin(\theta_\mathrm{h})$.

The acoustic radiation force on a particle can be determined from the gradient in the acoustic force potential[62] U, with

$$\boldsymbol{F}^{\mathrm{rad}} = -\nabla \mathrm{U} \qquad \text{Eqn. 10a}$$

$$\mathrm{U} = V_p\left[f_1\frac{1}{2}\kappa_0\langle p_1^2\rangle - f_2\frac{3}{4}\rho_0\langle v_1^2\rangle\right], \qquad \text{Eqn. 10b}$$

$$f_1 = 1 - \frac{\kappa_p}{\kappa_0}, \quad f_2 = 2\left(\rho_p - \rho_0\right)/\left(2\rho_p + \rho_0\right), \qquad \text{Eqn. 10c}$$

where $V_p = \frac{4\pi}{3}a^3$ is the particle volume, κ_p and ρ_p are the particle compressibility and density, and f_1 and f_2 are the monopole and dipole scattering coefficients. It is worth discussing the use of the Gor'kov equation as it has been shown elsewhere that it is only the imaginary components of the scattering coefficients that contribute to the acoustic radiation force in a plane travelling wave, yielding acoustic radiation forces along the propagation direction[63]. However, unlike a plane traveling wave, in the case of our system there are gradients in the acoustic field, and it is these which lead to particle motion. We also note that the force from a traveling wave force has been shown to be inconsequential for particles much smaller than the acoustic wavelength[33,40], instead the gradient effects dominate[64]. In a tightly focussed traveling wave acoustic beam, for example, it is the gradients in the sound field which pushes particles away from its centreline[65] in the same way particles are driven from antinodal

to nodal positions in a standing wave. The differences between conventional standing waves and the acoustic fields as presented here are that in a standing wave the gradients follow sinusoidal distributions, whereas there is no such limitation for field gradients arising from our spatially distributed traveling wave, and that for our SAW and fluid wavefronts the time average of the squared pressure and velocity components are spatially co-located; $\langle p_1^2 \rangle$ is at a maximum at the same location(s) as $\langle v_1^2 \rangle$. These differences, however, are readily accounted for in Equation 10 and in any case (regarding the spatial co-location of pressure and velocity maxima) do not have a significant effect on the calculated force since f_1 is approximately an order of magnitude larger than f_2 for dense particles in water.

Figure 5a examines the behaviour of U and the acoustic radiation forces experienced by suspended particles for the $\theta = 0°$ case. Particles experience no acoustic radiation force as defined in Equation 10 where the gradient of U is equal to zero. Though this is the case along all dashed lines in (i), only the black lines representing the local minima of U will retain particles, as any particle position perturbations at the local maxima (red dashed lines) will result in migration down acoustic force potential gradients. Note that $U > 0$ even in the acoustic fringe minima, as acoustic energy is still contained within the planar v_s wavefronts that interfere with the fluid wavelets (whose magnitudes given by v_c are uniformly smaller than v_s); it is the energy density gradient rather than its absolute magnitude that ultimately results in particle motion. These lines of zero U are equivalent to the iso-force lines mapped in (ii) of Figure 5a, where positive values are oriented in the $+x_{0°}$ direction; particles migrate due to both positive and negative forces along the direction force vector field $\boldsymbol{F}^{rad}$ towards the iso-force lines at potential field minima. Setting the fluid drag equal to the acoustic radiation force, the particle migration velocities are given by

$$\boldsymbol{v}_{\mathrm{p}} = \boldsymbol{F}^{rad}(6\pi\mu a)^{-1}, \qquad \text{Eqn. 11}$$

where $\boldsymbol{v}_\mathrm{p}$ is the particle velocity and μ is the fluid viscosity. The plot in (iii) of Figure 5a shows the magnitude and direction of particle migration according to the forces plotted in (ii). In a physical device with a channel roof, the acoustic field will necessarily be altered as partially reflected wave components will similarly result in acoustic force potential gradients in the *z*-direction, though by using a channel material such as the polydimethylsiloxane (PDMS) utilized here with only a ~4% reflection coefficient[58], the force and velocity magnitudes presented here are broadly representative of the rendered devices. In any event, the fringe spacing perpendicular to the channel walls is maintained. While the images here are representative of a particular set of specific particle properties (as stated in the Figure 5 caption), changes in the acoustic conditions will lead to different acoustic radiation force magnitudes without changes in the overall contour plot morphology, with $\xi \propto v_1$ and $\boldsymbol{v}_\mathrm{p} \propto \boldsymbol{F}^{rad} \propto \langle E \rangle \propto v_1^2$. For example, the maximum μm/s-order particle velocities shown in (iii) of Figure 5a for $U_1 = 0.15$ m/s would correspond to 100's of μm/s with $U_1 = 1.5$ m/s, where U_1 is the characteristic (initial, pre-attenuation) substrate displacement velocity.

Figure 5b shows plots of $\boldsymbol{F}^{rad}$ for wall orientations of $\theta = 0°$, 60°, 120° and 180°, where the fringe spacing along the x_θ direction matches the spacing predicted by Equation 2. Note that the SAW propagation direction is along the $+x$ direction, whereas these fringes are plotted along x_θ (Figure 5c). In (iv) of Figure 5b, for example, SAW wavefronts travel from right to left along the x_θ axis, representing the case where SAW wavefronts are travelling towards a channel wall placed in their path. The spacing is largest when the SAW wavefronts propagate in the same direction as the fluid wavelets ($\theta = 0°$), though the force magnitudes are largest when they are counter-propagating ($\theta = 180°$), owing to the larger acoustic force potential gradients occurring when the periodic spacing is smaller. Figure 5d shows that the fringe spacing (corresponding to the distance between iso-force locations) matches the predictions

from Equations 2 and 5, as measured by the distance between minima along the x_θ direction at $z = 1$ μm.

Because particle patterning is a result of acoustic radiation forces, we have omitted discussion of acoustic streaming, which will nevertheless occur and generate particle forces via fluid drag. The particular fluid velocities that result, however, are a function of the channel geometry; the relationship between this geometry, actuation mode, frequency, streaming velocity and their effects on particle migration have been discussed in detail elsewhere[14,32,43,56,59,66]. In the systems considered here, the acoustic radiation forces necessarily exceed those arising from fluid drag for particle patterning in acoustic fringes to be observed. We have ignored here also the effect of acoustic travelling waves on particle migration, as the effect of the stationary field is many orders of magnitude larger[67] when $R \ll \lambda$. Moreover, a travelling wave component would serve to drive denser particles in the direction of acoustic propagation, rather than create the observed fringe patterns. Having developed an analytical model that demonstrates the generation of acoustic forces resulting from a spatially limited transducer, we seek to demonstrate that these forces can be used to create fringe patterns in a physical system.

4. Methods

Each SAW device consists of a series of interdigitated transducer (IDT) electrodes patterned on a 128° *Y*-cut, *X*-propagating piezoelectric lithium niobate ($LiNbO_3$) substrate. A SAW device is characterised by its wavelength, λ_{SAW}, defined as the spacing between periodic IDT features. The applied harmonic frequency is such that the substrate deflections emanating from one set of IDT finger-pairs (at c_s) are reinforced by the neighbouring ones, with $f = c_\mathrm{s}/\lambda_{\mathrm{SAW}}$, and results in a travelling SAW on either side of a bidirectional IDT. To ensure maximum wavefront uniformity in the target region, the $\lambda_{\mathrm{SAW}} = 80$ μm IDTs used in this study are 14

mm wide, larger than the channel in which shaped channel features are placed. Wave absorber (First Contact Polymer, Photonic Cleaning Technologies, WI, USA) was used on the reverse side of the IDT and on the opposite side of the channel region to minimize spurious reflections. The 22-μm-high channel features were defined using conventional SU-8 photolithography (SU-8 2025, Microchemicals, Germany) and created from soft-lithographic polydimethylsiloxane (PDMS) moulding from the SU-8 master, whose patterns are shown in Figure S4. The completed channels were aligned and attached to the SAW device using plasma bonding (Harrick Plasma PDC-32G, NY). Fluorescent 1-μm-diameter polystyrene particles (Magsphere, CA) are used to trace the locations where both the acoustic radiation force is zero and the acoustic potential field is at a minimum, as shown by the black dashed lines in Figure 5a. A sound speed of 1540 m/s for the water-particle mixture is utilised in this work based on a 0.05% polystyrene particle volume fraction according to the Wood equation[68] and a 40 °C solution temperature. This temperature is based on thermal imaging measurements (FLIR i5, FLIR Systems Australia) and an applied power of 0.5 W.

Pressure fields are simulated according to a programmed implementation of the Huygens-Fresnel Principle, where the magnitude of the pressure field at a given point in the fluid is the integral of all spherical wave sources from the transducer plane. Channel walls enclosing a finite area affect the acoustic field within by spatially limiting the effective transducer area that can contribute to the pressure field. Accordingly, we simulate the effect of circular pillar-shaped channel walls by defining a masked circular region in which the substrate displacement is zero. This simulation process is described in detail in O'Rorke *et al*.[48]. Each contributing pixel in the transducer plane has dimensions of $1/50\lambda_{\mathrm{SAW}}$ in the *x* and *y*-directions, is simulated across a domain with dimensions of at least $12\lambda_{\mathrm{SAW}}$ by $12\lambda_{\mathrm{SAW}}$ and is evaluated immediately above the transducer plane (z = 1 μm) for a SAW wavelength of 80 μm. Each simulation removes

boundary effects in the fluid (i.e., that arising from the channel wall in the path of the SAW) by subtracting the pressure magnitude in the case where there is no simulated pillar feature.

5. Results and Discussion

In the results presented here we examine the interference patterns arising from channel features and compare with the predictions made in the analytical models. These patterns are visualized using polystyrene microparticles, which align at the acoustic force potential minima as shown in Figure 6. The experimental setup to test the predictions made by Equation 2 (and 5) is performed with flat channel interfaces that are set at select angles with respect to the SAW propagation direction. Figure 6 shows this periodicity near a channel wall placed in the path of a SAW. Figure 6a highlights the individual angles with interface orientations of 22.5°, 45°, 67.5°, 90°, 112.5°, 135° and 157°, each of which consists of a pair of 1,800 μm long, 160 μm wide PDMS channel walls that are bonded to the substrate at each of these orientations. The mean fringe spacing is calculated from the distances between maximum optical intensity peaks along the axis perpendicular to the interface, x_θ, with an example measurement shown in Figure 6a(viii). Error bars show ±1 standard deviation from the mean measured value. The spacings from Figure 6a are overlaid on the predictions from Equations 1 and 2 in Figure 6b, plotted as the ratio between the spatial periodicity at a given angle and the SAW wavelength ($\lambda_\theta \lambda_{\mathrm{SAW}}^{-1}$). Values of θ<90° are measured on the opposite pillar side (farther from the SAW source) and θ>90° are measured on the proximal side, as illustrated in the Figure 6c. Devendran *et al.* showed that the periodicity of the acoustic field evolves in the z-direction, as the acoustic energy maxima projects into the fluid at the Rayleigh angle θ_R (≈23° for $H_2O/LiNbO_3$) close to the channel interface and approaches $\theta_{\mathrm{nf}} = \frac{1}{2}\cos^{-1}\left[\frac{c_l}{c_s}\right]$ (≈34°) with increasing distance from it. Considering that a nodal position develops one half λ_l from the PDMS-water roof interface

in the z-direction, this results in an elongated periodicity at the trapping height. Therefore, Equations 1 and 2 have been accordingly modified to account for trapping of physical particles at a positive and finite position in the z-direction, with $\lambda_\theta = \lambda_{\theta(z=0)} + \varepsilon$. For a channel height of 22 μm, this predicted trapping height occurs at $z = 7$ μm, resulting in a difference (increase) of $\varepsilon = 1.7$ μm between these two angles at this height, or approximately 2% of λ_{SAW}; though the difference is small we include this correction factor for completeness when making comparisons with our experimental results. Comparing the flat and infinite curvature model predictions, the overall relationships between angle and periodic fringe spacing are similar, with increasing divergence for intermediate interface angles. The measured spacings in Figure 6 for flat channel features match well with the predictions from the flat wall model (Equations 2) and are uniformly higher than those predicted by Equation 1.

Whereas matching the flat wall condition from Equation 2 is straightforward to set up experimentally, the condition where $R \to 0$ is not, as the magnitude of the scattered wavefronts decreases with smaller values of $R\lambda_{SAW}^{-1}$. Accordingly, for Equation 1 to be probed experimentally the interface radius should be sufficiently large that particle aggregation can occur and so that effects from other channel walls, non-SAW wave components and reflections in the larger channel don not dominate particle migration behaviour. Though the patterning effect is less pronounced than in the flat wall case, it is still nevertheless observable for the entire 360° arc around a 400-μm-diameter cylinder interface, with $R\lambda_{\mathrm{SAW}}^{-1} = 2.5$, as shown in Figure 7a, albeit weakly for values of θ close to 0°. Figure 7b shows the modelled periodic patterning locations around this cylinder, with each subsequent patterning ellipsoid spaced λ_θ from the previous one for a given value of θ. Predicted patterns from Equations 1 and 2 are overlaid on the experimental condition in Figure 7c, in part to highlight their similarity and the difficulty in determining the exact value of λ_θ experimentally. Figure 7d shows the mean value

taken across three separate experiments for 10° increments in θ, where the error bars denote ±1 standard deviation from this value across all measured values for that angle. The inset shows optical intensity profiles for selected angles (θ = 0°, 90° and 180°). Though the sizable error bars are inherent for low scattering amplitudes with a channel interface radius on the order of λ_{SAW}, we can infer that their mean values are lower than both those measured in the case of a flat wall interface (Figure 6b) and the predictions from Equation 2. While these experimental conditions are valuable in demonstrating that wall interfaces subject to SAW yield consistent and robust patterning behaviour, the magnitude of the error bars (including for Figure 1b(i), whose measured periodicity is shown in Supplementary Figure S1) for these cases requires a more rigorous approach to comprehensively explore the effect of interface curvature.

Having established that our models are broadly predictive of acoustic periodicity in the experimental cases examined, we now examine the effect of channel interfaces in simulated and modelled conditions in which we can exclude effects imposed by heating, acoustic streaming, fluid flow, reflected waves, Brownian motion and unintended substrate vibration modes that may also modify the spatial force distribution on suspended particles in an experimental setup. Figure 8 shows the effect of increasing radial dimensions on the resulting periodicity, with representative simulation plots for $R = 0.1\lambda_{\mathrm{SAW}}$, $1\lambda_{\mathrm{SAW}}$, $4\lambda_{\mathrm{SAW}}$ and periodic fringe spacing plots for angles between 0° and 180°. These simulation images are chosen to demonstrate the change in fringe spacing with increasing channel pillar radius. The periodicity is assessed by measuring the distance between neighbouring peaks in the pressure amplitude profile along a specified angle at 0.1° intervals. At the lower limit ($R \to 0$) the simulated periodicity closely matches the case predicted by $\lambda_\theta^{(R\to 0)}$, with larger pillar dimensions increasing the resulting periodic spacing for a given value of θ; for $R = 0.1\lambda_{\mathrm{SAW}}$ the measured periodicity is equivalent to the equation for $\lambda_\theta^{(R\to 0)}$ whereas for $R = 4\lambda_{\mathrm{SAW}}$ it is intermediate

between the predictions from the equations for $\lambda_\theta^{(R\to 0)}$ and $\lambda_\theta^{(R\to\infty)}$ (Equations 1 and 2, respectively). While the relationship between periodic spacing and increasing R is apparent in these simulation results, which are useful in confirming the variation in periodic spacing as a function of θ as well as the increasing values of $\lambda_\theta^{(R\to\infty)}$ for increasing R, the measured periodic spacing does not clearly follow the predicted trendlines at values of θ closer to 0°, as shown in Supplementary Figure S5. This is ultimately a result of the interference lobes that can be seen in Figure 8, especially apparent for smaller values of θ. These arise from wave contributions on the near (SAW-source) side of the pillar; in the simulation the wavefield magnitude at every point in the field is computed as the sum of radially expanding wavefronts from every point on the substrate. Wavefronts propagate freely across the channel interfaces in the simulation and attenuation in the material is not considered, which is not the case experimentally. While this simulation model is useful in illustrating the bulk effects of a circular pillar wall on the surrounding acoustic field, an alternative model is required to clearly show the transition between Equation 1 and Equation 2 for increasing R.

Figure 9 introduces the results of such a model, which applies the Huygens-Fresnel principle to Equation 1; every point on the surface of the channel interface will result in its own interference ellipsoid owing to the circularly expanding fluid wavelets from that point. This model is illustrated graphically in Supplementary Figure S6, which shows that by arbitrarily decreasing the distance between neighbouring fluid wavelet point sources on the pillar, the distance between the pillar surface and where these ellipsoids maximally intersect can be readily determined. This is examined in a MATLAB model by plotting these ellipsoids along the edge of the interface. Using this model we can accurately examine periodicity evolution for increasing pillar radius. Figure 9a shows the transition between the predictive models where $\lambda_\theta^{(R\to 0)}$ and $\lambda_\theta^{(R\to\infty)}$, with increments of $0.1R\lambda_{SAW}^{-1}$, where $R\lambda_{SAW}^{-1}$ is the radius value normalized

by the SAW wavelength, between $0.1 \leq R\lambda_{SAW}^{-1} \leq 10$ and for sound speed ratios ($\tilde{c} = c_l/c_s$) of $\tilde{c} = 0.2, 0.4, 0.6$ and 0.8. The periodic spacing value $\lambda_\theta \lambda_{SAW}^{-1}$ is similarly normalized by the SAW wavelength. Notably, the difference between the predictive models is increased for intermediate values of θ and for $\tilde{c} \to 1$, and where increasing values of $R\lambda_{SAW}^{-1}$ result in values of λ_θ that asymptotically approach $\lambda_\theta^{(R\to\infty)}$. To examine the trajectories between these models as a function of $\tilde{c}$ more closely while isolating the effect $\tilde{c}$ has on the overall difference between Equation 1 and Equation 2, it is appropriate to determine the relative value of λ_θ between $\lambda_\theta^{(R\to 0)}$ and $\lambda_\theta^{(R\to\infty)}$. This relative value is given by

$$\tilde{\lambda}_\theta = \frac{\lambda_\theta - \lambda_\theta^{(R\to 0)}}{\lambda_\theta^{(R\to\infty)} - \lambda_\theta^{(R\to 0)}}. \qquad \text{Eqn. 12}$$

Figure 9b therefore examines the trajectory of $\tilde{\lambda}_\theta$ at the value of $\theta = 90°$ for increasing $\tilde{c}$. Regardless of the specific value of θ, however, the relationship between $\tilde{\lambda}_\theta$ and $\tilde{c}$ remains the same; values of c_l that approach c_s result in a less rapid shift from the $\lambda_\theta^{(R\to 0)}$ model to the $\lambda_\theta^{(R\to\infty)}$ one. This figure is important for determining the relative importance of Equations 1 and 2 for a given experimental case. In the case of the lithium niobate ($c_s = 3931$ m/s) and water combination used here, similar to $\tilde{c} = 0.4$, Equation 2 is broadly predictive of the periodicity for radii of curvature greater than $2\lambda_{SAW}$ ($\tilde{\lambda}_\theta \approx 0.8$). A slower propagation velocity in piezoelectric substrate materials such as polyvinylidene fluoride (PVDF, $c_s = 2200$ m/s, $\tilde{c} \approx 0.7$), however, requires a radius of $R > 6\lambda_{SAW}$ to yield a similar dominance of Equation 2 ($\tilde{\lambda}_\theta \approx 0.8$). Moreover, there is increasing discrepancy between the predictive models for larger values of $\tilde{c}$ generally; in this case it is important to use Equation 12 to generate periodicity predictions, especially for microchannel features whose dimensions are on the order of a few SAW wavelengths or less.

6. Conclusion

In this work we have demonstrated that channel interfaces placed in the path of a travelling SAW can produce robust interference patterns. We have further presented expressions to predict the spacing of these acoustic fringes, which are corroborated by an analytical model, experiments and simulations. Simulations and theoretical analysis based on the Huygens-Fresnel principle, in which spurious effects from streaming, reflections and secondary wave modes are avoided, provide evidence for the prediction that larger periodic spacings result as $R\lambda_{\mathrm{SAW}}^{-1} \to \infty$. The differences between the predictive models are increase for fluids with sound speeds approaching that of the underlying substrate, and thus are an important consideration when predicting periodic spacings, though amount to less than 10% for the combination of water on lithium niobate used in this study. While the aim of our present work is to demonstrate the appearance of acoustic fringe patterns near channel walls and to predict their spacing, effects such as acoustic streaming and their relative influence compared to other piezoelectric actuation methods besides SAW (e.g. Muller et al.)[66] is an interesting avenue for future work. We nevertheless show that diffractive patterning periodicity in microfluidic systems can be predicted based on novel physically-derived equations, with the predictions made by these equations (and the counter-intuitive result that patterning periodicity is a function of surface curvature) being supported by the confluence of the multitude of approaches that we have utilized. This includes calculation of acoustic fields in the x-z plane (Figure 5), experimental results in Figures 6 and 7, simulations in the x-y plane (Figure 8), and analysis of the transition behaviour between the derived analytical models (Eqns. 1 and 2). Taken together these present a comprehensive picture of 2D diffractive patterning activities in microfluidic systems in a way that has not been previously demonstrated.

This channel interface method for generating particle patterns has substantial advantages over conventional methods for generating acoustic radiation force fields with SAW, which typically create uniform standing waves across the entire IDT aperture. Because these interfaces can be placed arbitrarily within a microfluidic channel and their effect on the surrounding force field is spatially limited, these channel interfaces permit localized and flexible microfluidic manipulation. In comparison to recent work showing the generation of spatially localized acoustic fields in a pulsed SAW time-of-flight regime[30], channel interfaces permit force gradients at any angle to the SAW wavefront and with the imposition of only a single travelling wave. We expect this interface-based methodology to expand the range of acoustofluidic activities that can be performed on-chip. While the models developed in this work are specific to microfluidic devices actuated by SAW, our approach of applying Huygens-Fresnel principles has wider utility in providing future predictions for diffractive-based acoustic micromanipulation in other systems.

Acknowledgement

We gratefully acknowledge the support received from Singapore Ministry of Education Academic Research Fund Tier 2 (T2MOE1603) awarded to Y.A. D. C. was partially supported by SUTD-MIT joint postdoctoral fellowship.

7. Figures

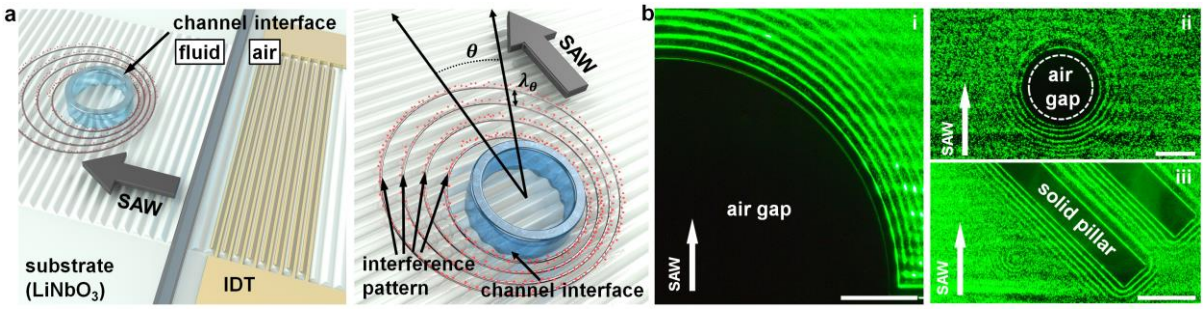

Figure 1: Interference in the vicinity of a channel interface produces patterning phenomena. (a) Concept image, where an incident surface acoustic wave (SAW) arising from an interdigitated transducer interacts with a channel interface to produce an interference pattern with periodicity λ_θ. (b) Experimental 1 µm microparticle patterning from a (i) semicircle, (ii) circle (iii) and rectangular channel interfaces. PDMS-air interfaces are denoted by a dashed white line. Scale bar is 200 µm.

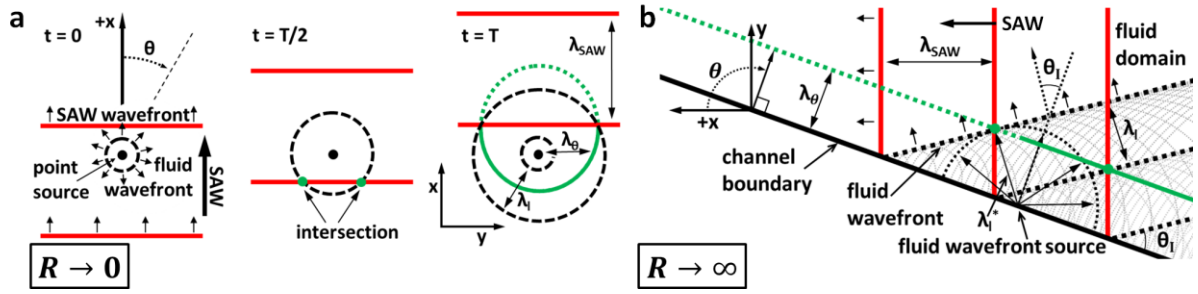

Figure 2: Interference models for Equations 1 and 2, respectively. (a) In the case where the radius R of the interface is much smaller than the acoustic wavelength ($R \rightarrow 0$) the scattered fluid wavefront (dashed black line) intersects with the fluid wavefront arising from the SAW (red line) to produce an ellipsoidal interference pattern (green line). This intersection is demonstrated in Supplementary Video 1. (b) In the case of a flat channel interface ($R \rightarrow \infty$) the fluid wavefronts similarly intersect with the planar SAW wavefronts in the fluid to produce an interference pattern parallel to the interface.

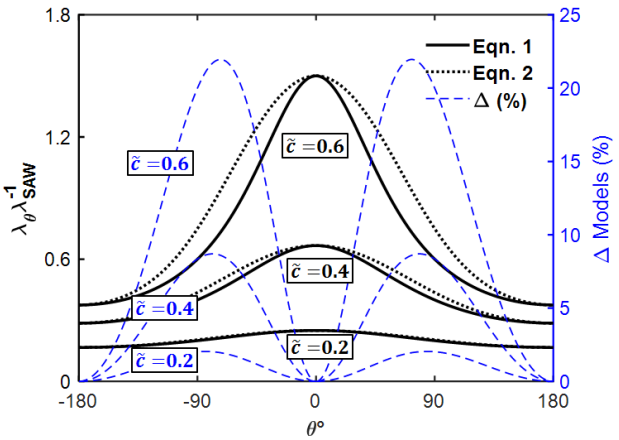

Figure 3: Periodic spacing near a channel interface for models in the case where $R \rightarrow 0$ (Eqn. 1) and $R \rightarrow \infty$ (Eqn. 2) plotted for values of $\tilde{c} = 0.2, 0.4$ and 0.6. Dashed blue line denotes the percentage difference between these models with θ, whose magnitude increases as $\tilde{c}$ approaches unity.

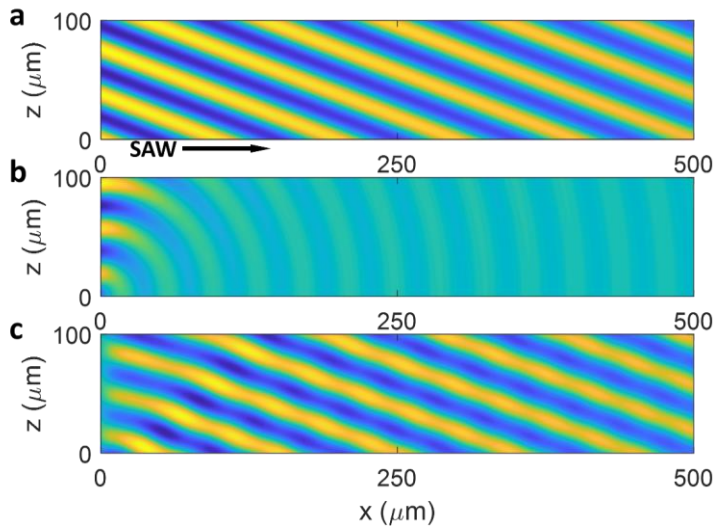

Figure 4: First order transient acoustic pressures in the *x*-*z* plane arising from the velocities in (a) Eqn. 11 and (b) Eqn. 13, where (c) shows the sum of these pressures, with $p_s + p_c$. This results in visible diffraction lobes in the combined field in the fluid domain. These plots are for $\lambda_{SAW} = 100$ μm, $\theta = 0$ and a channel wall at $x = 0$, where in these arbitrarily scaled images the yellow represents the maximum pressure condition and the blue is the minimum pressure. Each SAW wavefront creates a new fluid wavelet in (b) as it enters the channel. These wavefronts are animated in Supplementary Video 2.

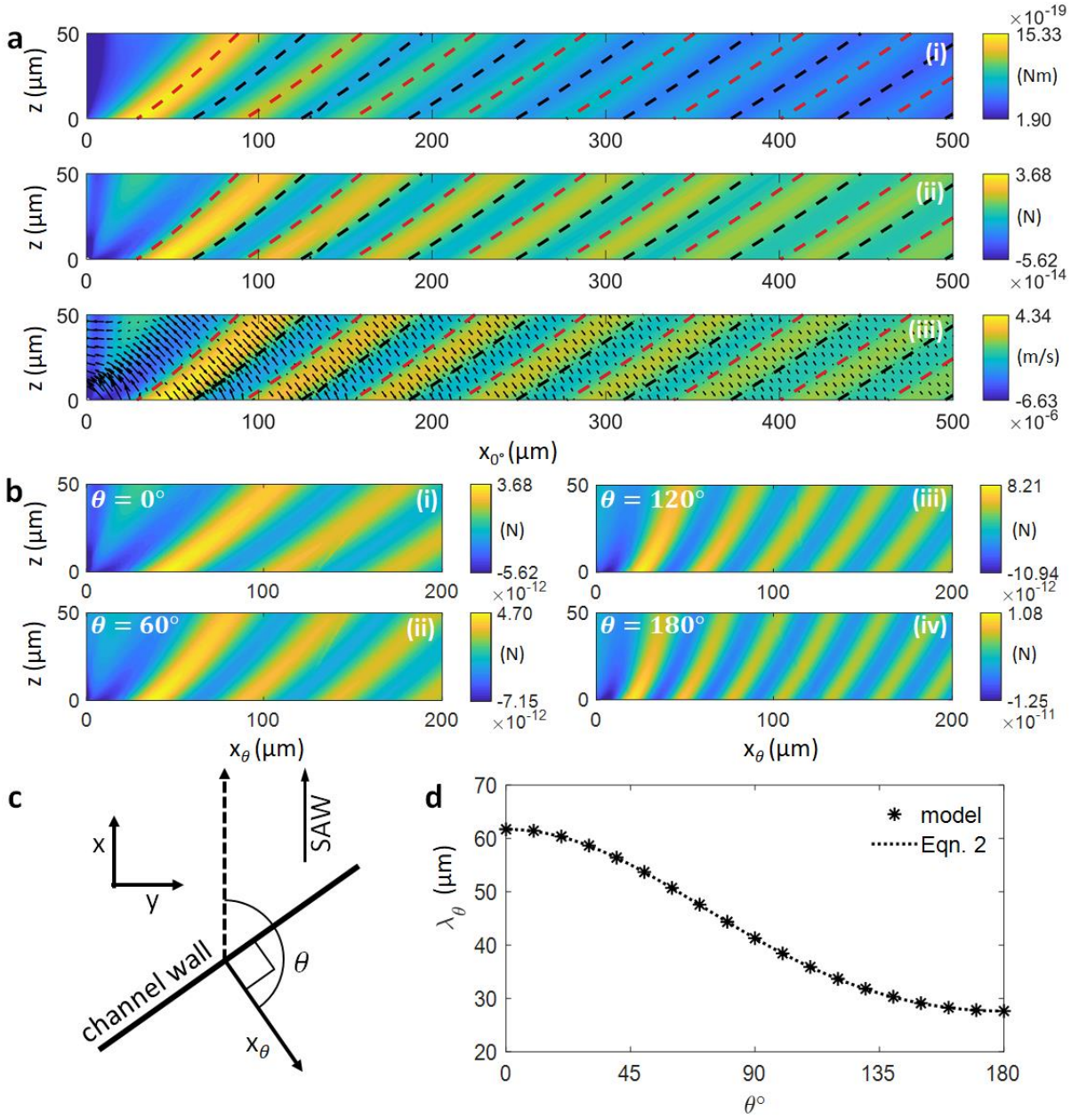

Figure 5: Acoustic field in the x-z plane orthogonal to channel wall in the fluid domain. (a) The acoustic force potential U in (i) follows the contours of time-averaged energy density, $\langle E \rangle$, where lines of maximum and minimum U are marked in red and black, respectively. (ii) F^{rad}, with plotted lines from (i) corresponding here to F^{rad} = 0 contours. (iii) Particle velocity plot, where arrows point in the direction of particle migration. Plots are for a 1 μm polystyrene particle diameter (ρ_p = 1050 kg/m^3, κ_p = 2.5E-10 Pa^{-1}), μ = 9E-4 Pa·s, a maximum fluid particle velocity $U_1 = \omega\xi_0$ of 0.15 m/s and λ_{SAW} = 100 μm, with $\theta = 0°$. (b) Plots of F^{rad} (in Newtons) on a 1 μm polystyrene particle for different θ; these are 0°, 60°, 120° and 180° in (i)-(iv), respectively. (c) Each contour plot is mapped along the x-axis x_θ, defined as the axis perpendicular to the channel wall. (d) The fringe spacing (from minima to minima) along x_θ from this model matches the spacing from Equations 2&5.

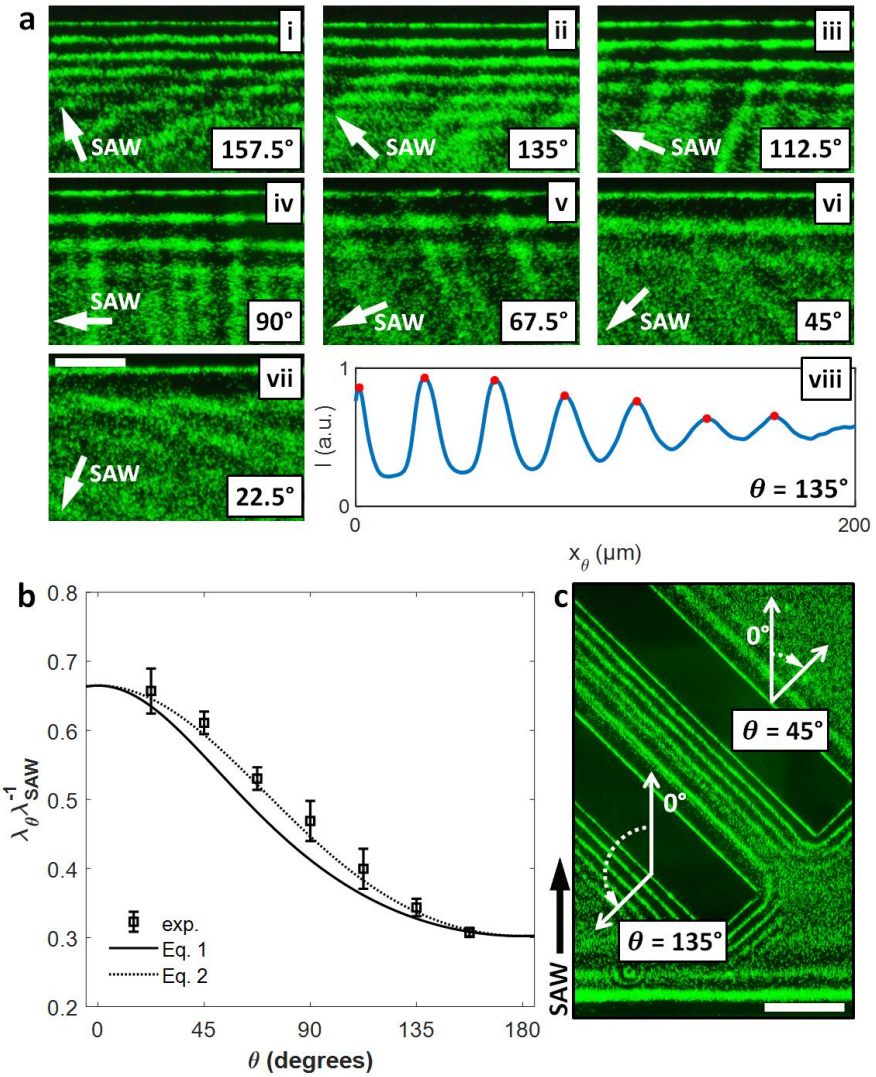

Figure 6: Patterning spacing in near a flat wall. (a) Experimental images rotated to the channel wall frame of reference. White arrow shows the orientation of the underlying travelling SAW, here for wall angles of (i) 157.5°, (ii) 135°, (iii) 112.5°, (iv) 90°, (v) 67.5°, (vi) 45° and (vii) 22.5°. Scale bar (in bottom left image) is 100 μm. The figure in (viii) shows the optical intensity for an example measurement (135°), with red dots at each measured peak. The intensity values are computed as the average of the horizontal pixels in each of (i-vii). (b) Taking measurements of these spacings for each angle in (a) we compare these results with Equations 1 and 2. The error bars here represent one standard deviation of the measured spacings (i.e. the distances between red dots in a(viii)). (c) One set of pillars is used to make two measurements on either side, here showing an example at 45° and 135°. The value for θ is measured from the SAW propagation direction (θ = 0°). Scale bar is 200 μm.

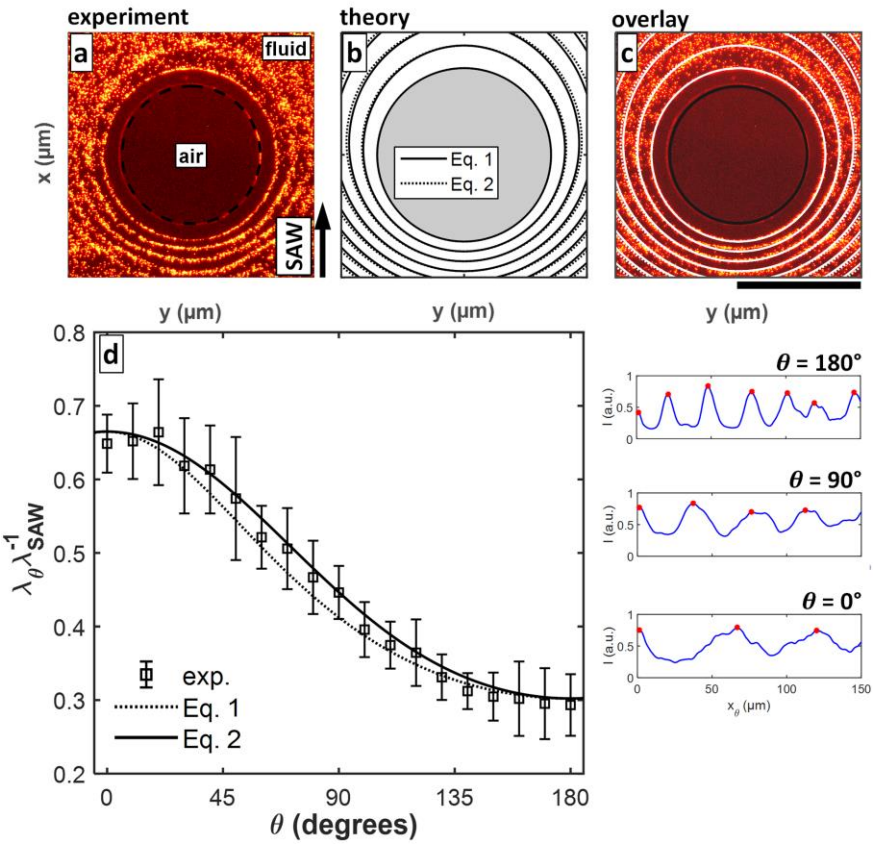

Figure 7: Periodic spacing in the vicinity of a circular feature. (a) A SAW produces an ellipsoidal interference pattern near a circular channel interface. Black dashed line denotes internal (air-filled) channel boundary. (b) The predicted periodicity from Eqn. 1 and 2 from a circular channel interface (interior colored gray) with a diameter of 400 μm, and (c) overlaid on the image in (a). Scalebar is 300 μm. (d) The measured periodicity for this intermediate sized-object is between the two predictive models, which are for the extremes of a pillar with $R \rightarrow 0$ (Eqn. 1) and a flat interface (Eqn. 2). The error bars here represent one standard deviation of the measured spacings (i.e. the distances between red dots in graphs at right). Right graphs show three representative optical intensity profiles measured from the edge of the interface (at θ = 0°, 90° and 180°).

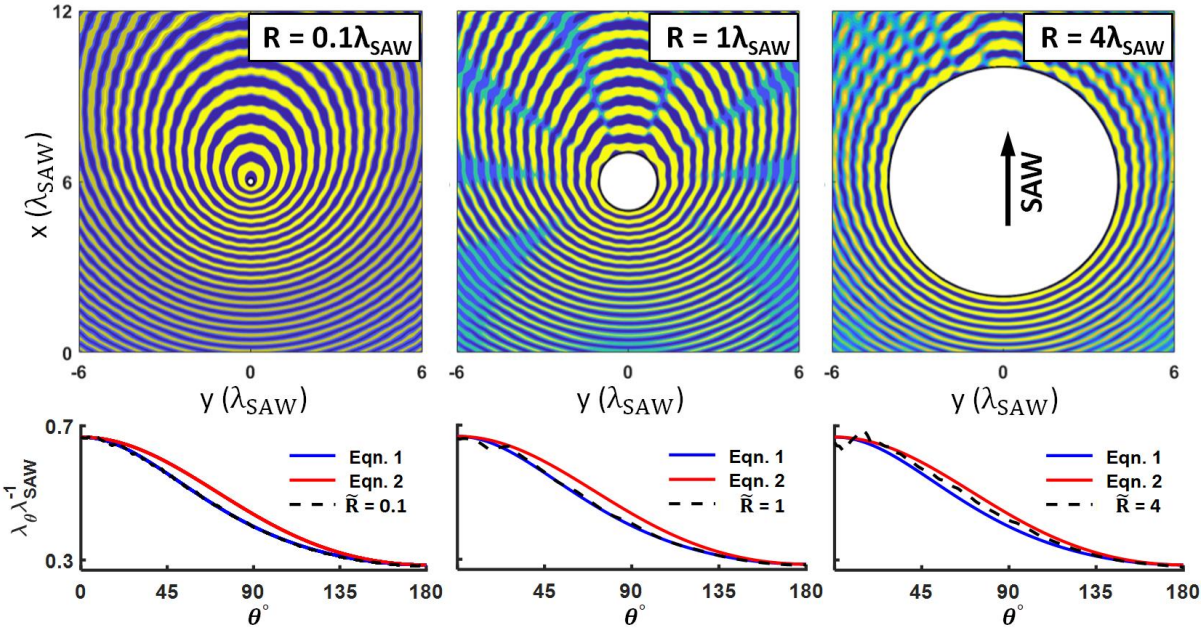

Figure 8: Simulated periodicity in the fluid domain. Pressure field $\langle p_1^2 \rangle$ resulting from a circular pillar interface (white circle) in the path of a travelling SAW for pillar radius $R = (0.1, 1, 4)\lambda_{\mathrm{SAW}}$ for the case where c_l/c_s = 0.4. Graphs below each simulation figure plot the periodicity from each of these for $0^\circ \leq \theta \leq 180^\circ$.

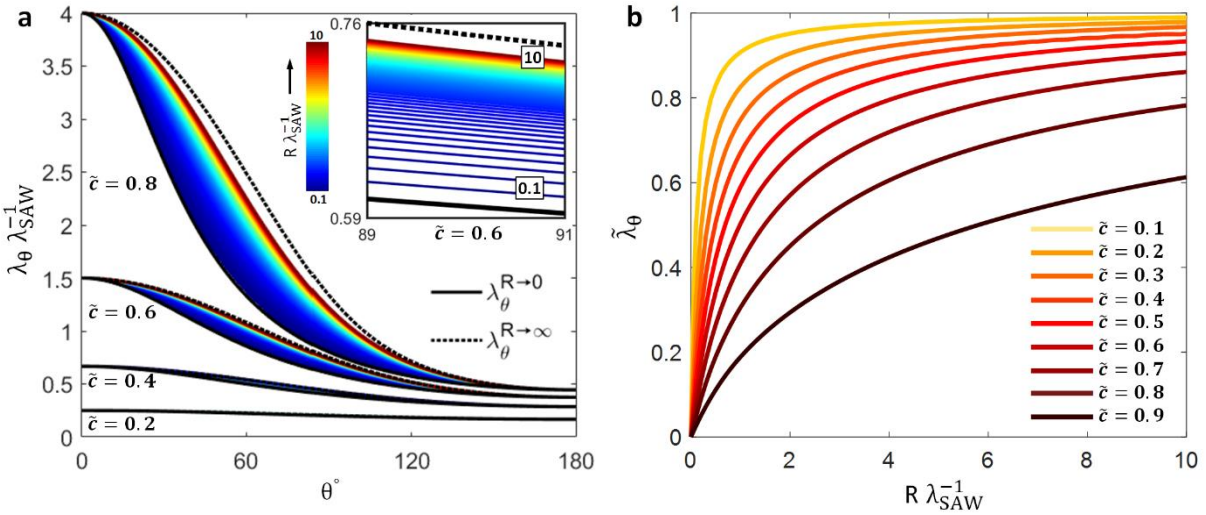

Figure 9: Effect of sound speed on transition between Eqn. 1 and Eqn. 2. (a) Plot of periodicity for pillar elements with $R = 0.1\lambda_{SAW}$ to $R = 10\lambda_{SAW}$ in increments of $0.1\lambda_{SAW}$, for sound speed ratios $\tilde{c} = c_l/c_s = 0.2, 0.4, 0.6$ and 0.8. Inset shows increasing periodic lengths for for increasing $R\lambda_{SAW}^{-1}$, here for $\tilde{c} = 0.6$. (b) The modelled transition rate between the two extreme cases (where $\tilde{\lambda}_\theta = 0$ and $\tilde{\lambda}_\theta = 1$ corresponds to $\lambda_\theta^{R\to 0}$ [Equation 1] and $\lambda_\theta^{R\to\infty}$ [Equation 2]) decreases as $\tilde{c} \to 1$, here examined for $\theta = 90°$. These spacings are obtained from the model methodology outlined in Supplementary Figure S4.

8. References

1. Tian, L. *et al.* Spontaneous assembly of chemically encoded two-dimensional coacervate droplet arrays by acoustic wave patterning. *Nat. Commun.* **7**, 13068 (2016).

2. Naseer, S. M. *et al.* Surface acoustic waves induced micropatterning of cells in gelatin methacryloyl (GelMA) hydrogels. *Biofabrication* **9**, 15020 (2017).
3. Oberti, S., Neild, A. & Dual, J. Manipulation of micrometer sized particles within a micromachined fluidic device to form two-dimensional patterns using ultrasound. *J. Acoust. Soc. Am.* **121**, 778–785 (2007).
4. Ma, Z., Zhou, Y., Collins, D. J. & Ai, Y. Fluorescence activated cell sorting via a focused traveling surface acoustic beam. *Lab Chip* **17**, 3176–3185 (2017).
5. Nawaz, A. A. *et al.* Acoustofluidic fluorescence activated cell sorter. *Anal. Chem.* **87**, 12051–12058 (2015).
6. Schmid, L., Weitz, D. A. & Franke, T. Sorting drops and cells with acoustics: acoustic microfluidic fluorescence-activated cell sorter. *Lab Chip* **14**, 3710–3718 (2014).
7. Ung, W. L. *et al.* Enhanced surface acoustic wave cell sorting by 3D microfluidic-chip design. *Lab Chip* **17**, 4059–4069 (2017).
8. Destgeer, G. *et al.* Acoustofluidic particle manipulation inside a sessile droplet: four distinct regimes of particle concentration. *Lab Chip* **16**, 660–667 (2016).
9. Ma, Z., Collins, D. J. & Ai, Y. Detachable Acoustofluidic System for Particle Separation via a Traveling Surface Acoustic Wave. *Anal. Chem.* (2016). doi:10.1021/acs.analchem.6b00605
10. Wang, S. *et al.* Flexible Piezoelectric Fibers for Acoustic Sensing and Positioning. *Adv. Electron. Mater.* **3**, (2017).
11. Collins, D. J. *et al.* Selective particle and cell capture in a continuous flow using micro-vortex acoustic streaming. *Lab Chip* **17**, 1769–1777 (2017).
12. Ahmed, H., Destgeer, G., Park, J., Jung, J. H. & Sung, H. J. Vertical Hydrodynamic Focusing and Continuous Acoustofluidic Separation of Particles via Upward Migration. *Adv. Sci.* **5**, (2018).
13. Shilton, R. J., Travagliati, M., Beltram, F. & Cecchini, M. Microfluidic pumping through miniaturized channels driven by ultra-high frequency surface acoustic waves. *Appl. Phys. Lett.* **105**, (2014).
14. Collins, D. J., Ma, Z., Han, J. & Ai, Y. Continuous micro-vortex-based nanoparticle manipulation via focused surface acoustic waves. *Lab Chip* **17**, 91–103 (2017).
15. Ahmed, D. *et al.* Focusing of sub-micrometer particles and bacteria enabled by two-dimensional acoustophoresis. *Lab Chip* **6**, 7069 (2016).
16. Riaud, A., Baudoin, M., Bou Matar, O., Becerra, L. & Thomas, J.-L. Selective Manipulation of Microscopic Particles with Precursor Swirling Rayleigh Waves. *Phys. Rev. Appl.* **7**, (2017).
17. Baudoin, M. *et al.* Folding a focalized acoustical vortex on a flat holographic transducer: miniaturized selective acoustical tweezers. *Sci. Adv.* **5**, eaav1967 (2019).
18. Wiklund, M. Acoustofluidics 12: Biocompatibility and cell viability in microfluidic acoustic resonators. *Lab Chip* **12**, 2018 (2012).
19. Jonnalagadda, U. S. *et al.* Acoustically modulated biomechanical stimulation for human cartilage tissue engineering. *Lab Chip* **18**, 473–485 (2018).
20. Kurashina, Y., Takemura, K. & Friend, J. Cell agglomeration in the wells of a 24-well plate using acoustic streaming. *Lab Chip* **17**, 876–886 (2017).
21. Skowronek, V., Rambach, R. W. & Franke, T. Surface acoustic wave controlled integrated band-pass filter. *Microfluid. Nanofluidics* **19**, 335–341 (2015).
22. Rezk, A. R., Ramesan, S. & Yeo, L. Y. Plug-and-actuate on demand: multimodal individual addressability of microarray plates using modular hybrid acoustic wave technology. *Lab Chip* **18**, 406–411 (2018).
23. Rambach, R. W. *et al.* Visualization of Surface Acoustic Waves in Thin Liquid Films. *Sci. Rep.* **6**, (2016).
24. Destgeer, G., Lee, K. H., Jung, J. H., Alazzam, A. & Sung, H. J. Continuous separation of particles in a PDMS microfluidic channel via travelling surface acoustic waves (TSAW). *Lab Chip* **13**, 4210–4216 (2013).
25. Rezk, A. R., Manor, O., Friend, J. R. & Yeo, L. Y. Unique fingering instabilities and soliton-like wave propagation in thin acoustowetting films. *Nat. Commun.* **3**, (2012).
26. Li, S. *et al.* Standing surface acoustic wave based cell coculture. *Anal. Chem.* **86**, 9853–9859 (2014).

27. Orloff, N. D. *et al.* Manipulating particle trajectories with phase-control in surface acoustic wave microfluidics. *Biomicrofluidics* **5**, (2011).
28. Bernard, I. *et al.* Controlled rotation and translation of spherical particles or living cells by surface acoustic waves. *Lab Chip* **17**, 2470–2480 (2017).
29. Guo, F. *et al.* Three-dimensional manipulation of single cells using surface acoustic waves. *Proc. Natl. Acad. Sci. U. S. A.* **113**, 1522–1527 (2016).
30. Collins, D. J. *et al.* Acoustic tweezers via sub–time-of-flight regime surface acoustic waves. *Sci. Adv.* **2**, e1600089 (2016).
31. Salehi-Reyhani, A. *et al.* Chemical-free lysis and fractionation of cells by use of surface acoustic waves for sensitive protein assays. *Anal. Chem.* **87**, 2161–2169 (2015).
32. Tiller, B., Reboud, J., Tassieri, M., Wilson, R. & Cooper, J. M. Frequency dependence of microflows upon acoustic interactions with fluids. *Phys. Fluids* **29**, (2017).
33. Skowronek, V., Rambach, R. W., Schmid, L., Haase, K. & Franke, T. Particle deflection in a poly(dimethylsiloxane) microchannel using a propagating surface acoustic wave: Size and frequency dependence. *Anal. Chem.* **85**, 9955–9959 (2013).
34. Ahmed, D. *et al.* Rotational manipulation of single cells and organisms using acoustic waves. *Nat. Commun.* **7**, 11085
35. Ahmed, D. *et al.* Selectively manipulable acoustic-powered microswimmers. *Sci. Rep.* **5**, 9744 (2015).
36. Karlsen, J. T., Augustsson, P. & Bruus, H. Acoustic Force Density Acting on Inhomogeneous Fluids in Acoustic Fields. *Phys. Rev. Lett.* **117**, (2016).
37. Baasch, T. & Dual, J. Acoustofluidic particle dynamics: Beyond the Rayleigh limit. *J. Acoust. Soc. Am.* **143**, 509–519 (2018).
38. Liang, S. & Chaohui, W. Acoustic radiation force on a compressible cylinder in the standing surface acoustic wave (SSAW). *J. Appl. Phys.* **123**, (2018).
39. Habibi, R., Devendran, C. & Neild, A. Trapping and patterning of large particles and cells in a 1D ultrasonic standing wave. *Lab Chip* **17**, 3279–3290 (2017).
40. Ma, Z., Collins, D. J. & Ai, Y. Single-actuator Bandpass Microparticle Filtration via Traveling Surface Acoustic Waves. *Colloids Interface Sci. Commun.* **16**, 6–9 (2017).
41. Park, K. *et al.* In-droplet microparticle separation using travelling surface acoustic wave. *Biomicrofluidics* **11**, 64112 (2017).
42. Ng, J. W., Collins, D. J., Devendran, C., Ai, Y. & Neild, A. Flow-rate-insensitive deterministic particle sorting using a combination of travelling and standing surface acoustic waves. *Microfluid. Nanofluidics* **20**, (2016).
43. Kiebert, F. *et al.* 3D measurement and simulation of surface acoustic wave driven fluid motion: A comparison. *Lab Chip* **17**, 2104–2114 (2017).
44. Devendran, C., Albrecht, T., Brenker, J., Alan, T. & Neild, A. The importance of travelling wave components in standing surface acoustic wave (SSAW) systems. *Lab Chip* **16**, 3756–3766 (2016).
45. Devendran, C., Collins, D. J., Ai, Y. & Neild, A. Huygens-Fresnel acoustic interference and the development of robust time-averaged patterns from traveling surface acoustic waves. *Phys. Rev. Lett.* **118**, 154501 (2017).
46. Collins, D. J. *et al.* Self-Aligned Acoustofluidic Particle Focusing and Patterning in Microfluidic Channels from Channel-Based Acoustic Waveguides. *Phys. Rev. Lett.* **120**, (2018).
47. Collins, D. J. *et al.* Self-Aligned Acoustofluidic Particle Focusing and Patterning in Microfluidic Channels from Channel-Based Acoustic Waveguides. *Phys. Rev. Lett.* **120**, 74502 (2018).
48. O'Rorke, R., Collins, D. & Ai, Y. A rapid and meshless analytical model of acoustofluidic pressure fields for waveguide design. *Biomicrofluidics* **12**, (2018).
49. Leibacher, I., Schatzer, S. & Dual, J. Impedance matched channel walls in acoustofluidic systems. *Lab Chip* **14**, 463–470 (2014).
50. Bian, Y. *et al.* Acoustofluidic waveguides for localized control of acoustic wavefront in microfluidics. *Microfluid. Nanofluidics* **21**, (2017).
51. Rambach, R. W., Skowronek, V. & Franke, T. Localization and shaping of surface acoustic

waves using PDMS posts: Application for particle filtering and washing. *RSC Adv.* **4**, 60534–60542 (2014).
52. Li, P. *et al.* Detachable Acoustophoretic System for Fluorescence Activated Sorting at Single Droplet Level. *Anal. Chem.* (2019).
53. Weight, J. P. & Hayman, A. J. Observations of the propagation of very short ultrasonic pulses and their reflection by small targets. *J. Acoust. Soc. Am.* **63**, 396–404 (1978).
54. Hayman, A. J. & Weight, J. P. Transmission And Reception Of Short Ultrasonic Pulses By Circular And Square Transducers. *J. Acoust. Soc. Am.* **66**, 945–951 (1979).
55. Collins, D. J. *et al.* Atomization off thin water films generated by high-frequency substrate wave vibrations. *Phys. Rev. E - Stat. Nonlinear, Soft Matter Phys.* **86**, 056312 (2012).
56. Collins, D. J., Ma, Z. & Ai, Y. Highly localized acoustic streaming and size-selective submicrometer particle concentration using high frequency microscale focused acoustic fields. *Anal. Chem.* **88**, 5513–5522 (2016).
57. Holmes, M. J., Parker, N. G. & Povey, M. J. W. Temperature dependence of bulk viscosity in water using acoustic spectroscopy. in *Journal of Physics: Conference Series* **269**, 012011 (IOP Publishing, 2011).
58. Collins, D. J., Neild, A. & Ai, Y. Highly focused high-frequency travelling surface acoustic waves (SAW) for rapid single-particle sorting. *Lab Chip* **16**, 471–479 (2016).
59. Dentry, M. B., Yeo, L. Y. & Friend, J. R. Frequency effects on the scale and behavior of acoustic streaming. *Phys. Rev. E - Stat. Nonlinear, Soft Matter Phys.* (2014). doi:10.1103/PhysRevE.89.013203
60. Rappaport, T. S. *Wireless communications: principles and practice*. **2**, (prentice hall PTR New Jersey, 1996).
61. Makanjuola, N. T., Akinyemi, L. A., Shoewu, O. O. & Ojeyemi, F. O. Analysis of Diffraction Losses Using the Geometric Theory of Diffraction (GTD) over Varying Heights.
62. Gor'Kov, L. P. On the forces acting on a small particle in an acoustical field in an ideal fluid. in *Sov. Phys. Dokl.* **6**, 773–775 (1962).
63. Settnes, M. & Bruus, H. Forces acting on a small particle in an acoustical field in a viscous fluid. *Phys. Rev. E - Stat. Nonlinear, Soft Matter Phys.* **85**, 016327 (2012).
64. Fakhfouri, A. *et al.* Surface acoustic wave diffraction driven mechanisms in microfluidic systems. *Lab Chip* **18**, 2214–2224 (2018).
65. Collins, D. J. & Ai, Y. Detachable Acousto fluidic System for Particle Separation via a Traveling Surface Acoustic Wave. (2016). doi:10.1021/acs.analchem.6b00605
66. Muller, P. B., Barnkob, R., Jensen, M. J. H. & Bruus, H. A numerical study of microparticle acoustophoresis driven by acoustic radiation forces and streaming-induced drag forces. *Lab Chip* **12**, 4617–4627 (2012).
67. Qi, Q. & Brereton, G. J. Mechanisms of removal of micron-sized particles by high-frequency ultrasonic waves. *IEEE Trans. Ultrason. Ferroelectr. Freq. Control* **42**, 619–629 (1995).
68. Chambre, P. L. Speed of a Plane Wave in a Gross Mixture. *J. Acoust. Soc. Am.* **26**, 329–331 (1954).